Seismic Imaging of Rapid Onset of Stratified Turbulence in the South Atlantic Ocean

Matthew Falder*

Bullard Laboratories, Department of Earth Sciences, University of Cambridge, Cambridge, UK

N. J. White

Bullard Laboratories, Department of Earth Sciences, University of Cambridge, Cambridge, UK

C. P. Caulfield

BP Institute & Department of Applied Mathematics & Theoretical Physics, University of Cambridge, Cambridge, UK

**Corresponding author address:* Bullard Laboratories, Madingley Rise, Madingley Road, Cambridge, CB3 0EZ, UK

E-mail: maf49@cam.ac.uk, njw10@cam.ac.uk, cpc12@cam.ac.uk

ABSTRACT

Broadband measurements of the internal wavefield will help to unlock an understanding of the energy cascade within the oceanic realm. However, there are challenges in acquiring observations with sufficient spatial resolution, especially in horizontal dimensions. Seismic reflection profiling can achieve a horizontal and vertical resolution of order meters. It is suitable for imaging thermohaline fine structure on scales that range from tens of meters to hundreds of kilometers. This range straddles the transition from internal wave to turbulent regimes. Here, we analyze an 80 km long seismic image from the Falkland Plateau and calculate vertical displacement spectra of tracked reflections. First, we show that these spectra are consistent with the Garrett-Munk model at small horizontal wavenumbers (i.e. $k_x \lesssim 3 \times 10^{-3}$ cpm). There is a transition to stratified turbulence at larger wavenumbers (i.e. $k_x \gtrsim 2 \times 10^{-1}$ cpm). This transition occurs at length scales that are significantly larger than the Ozmidov length scale above which stratification is expected to modify isotropic Kolmogorov turbulence. Secondly, we observe a rapid onset of this stratified turbulence over a narrow range of length scales. This onset is consistent with a characteristic energy injection scale of stratified turbulence with a forward cascade toward smaller scales through isotropic turbulence below the Ozmidov length scale culminating in microscale dissipation. Finally, we estimate the spatial pattern of diapycnal diffusivity and show that the existence of an injection scale can increase these estimates by a factor of two.

1. Introduction

The oceanic internal wavefield probably arises from a forward cascade of energy from large-scale to small-scale processes (Thorpe 2005). Spectral analysis of this wavefield has played a useful role in developing quantitative models. For example, the power spectrum of vertical density displacements as a function of horizontal wavenumber, $\phi_\zeta(k_x)$, shows that distinctive regimes exist with different spectral slopes. At $k_x < 5 \times 10^{-3}$ cpm, corresponding to length scales of $> O(10^2\text{–}10^3)$ m, the Garrett-Munk model provides an accurate empirical description of the behavior of internal waves (Garrett and Munk 1975). At higher values of k_x, a transition into what is conventionally assumed to be a turbulent regime is observed (Figure 1). This transition is generally attributed to breaking of internal waves and to different kinds of convective and/or shear instabilities that can occur within a stratified fluid. In this turbulent regime, $\phi_\zeta(k_x)$ varies as a function of $k_x^{-5/3}$ which distinguishes it from the internal wave regime. At sufficiently small length scales, an exponent of $-5/3$ is consistent with an inertial convective sub-range that is based upon isotropic turbulent models (Kolmogorov 1941; Obukhov 1949; Corrsin 1951; Batchelor et al. 1959).

It is increasingly evident that flow at horizontal length scales of $O(10^2)$ m within a sufficiently stratified fluid does not always satisfy the underlying assumptions of these canonical models (Lindborg 2006; Riley and Lindborg 2008). For example, at horizontal scales greater than the Ozmidov length scale, l_O, overturning can be strongly suppressed and the fundamental properties of turbulence are moderated by stratification. l_O is given by

$$l_O = \left(\frac{\varepsilon}{N^3}\right)^{1/2}, \tag{1}$$

where ε is the dissipation rate of turbulent kinetic energy per unit mass and N is the buoyancy frequency given by

$$N^2 = -\frac{g}{\rho}\frac{\partial \rho}{\partial z}, \tag{2}$$

where ρ is potential density.

Since l_O is typically $O(10^{-2}$–$10^0)$ m, it is reasonable to infer that larger scales are associated with anisotropic flow, which fundamentally differ from that postulated by the Obukhov-Corrsin model (Gargett and Hendricks 1981). Horizontal flow is unconstrained by a stabilizing buoyancy force and so vertical fluctuations are expected to be smaller than horizontal fluctuations. Lindborg (2006) suggested that a horizontal energy spectrum with a power-law exponent of $-5/3$ is energetically consistent with a strongly anisotropic inertial flow regime which is perhaps confusingly referred to as 'stratified turbulence' (Riley and Lindborg 2010). In order to discriminate between turbulence within a stratified regime and stratified turbulence, we use the term layered anisotropic stratified turbulence (LAST) to define the regime referred to by Lindborg (2006). The existence of this LAST regime is supported by reinterpretation of published observations and by numerical simulations (Riley and Lindborg 2008; Brethouwer et al. 2007).

Here, we describe and analyze a seismic reflection experiment from the Falkland Plateau in the South Atlantic Ocean. Records from this experiment are used to construct a vertical image of the water column which reveals the detailed thermohaline structure at equal horizontal and vertical resolutions. We have four principal aims. First, we wish to demonstrate that meaningful information about the internal wave and turbulent regimes can be extracted by careful processing of seismic reflection datasets. In this regard, our approach builds upon and complements the analysis and recommendations of Holbrook et al. (2013). Secondly, spectral analysis of vertical displacements of undulating reflections is carried out in order to investigate internal wave and turbulent regimes as a function of horizontal wavenumber (Holbrook and Fer 2005). Thirdly, we use averaging and normalization methods to investigate the nature of the transition between internal waves and turbulence that has significant fluid dynamical implications. Fourthly, we estimate the spatial distribution of mixing and dissipation along a seismic image (Sheen et al. 2009; Holbrook et al.

2013). This approach complements global calculations made using one-dimensional microstructure profiling (e.g. Waterhouse et al. 2014).

2. Seismic Imaging of Thermohaline Structure

Seismic reflection experiments use a controlled source to make well-resolved images of the Earth's sub-surface. Acoustic energy is generated by priming tuned arrays of airguns with compressed air. These arrays are repeatedly fired to expel regular pulses of compressed air into the water column. Such arrays have total volumes of > 150 liters and the vertically directed acoustic energy has a typical frequency bandwidth of 10–200 Hz. Energy from each pulse is transmitted through the sub-surface and reflected at impedance contrasts. In the oceans, these contrasts are produced by temperature contrasts as small as 0.03°C over a few meters (Nandi et al. 2004). Salinity generally makes a minor contribution (Sallarès et al. 2009). Reflected acoustic energy is recorded by a towed streamer of hydrophones that is typically 2–12 km long. Since the reflected energy has a low signal-to-noise ratio, each point in the sub-surface is recorded multiple times over a period of tens of minutes. This sampling redundancy enables signal stacking which is used to improve the signal-to-noise ratio. Following Holbrook et al. (2013), we estimate the signal-to-noise ratio for two adjacent seismograms to be

$$\frac{S}{N} = \sqrt{\frac{|c|}{|a-c|}} \tag{3}$$

where c is the maximum value of the cross-correlation of both traces and a is the zero-lag autocorrelation of the first trace.

Although seismic reflection technology was developed to image the solid Earth, Holbrook et al. (2003) demonstrated that this technology is eminently suitable for mapping thermohaline fine structure. In a typical two-dimensional seismic experiment, vertical slices extending from the sea surface down to the sea bed are acquired. The 80 km long seismic image analyzed here is located ~ 100 km east of the Falkland Islands in the South Atlantic Ocean (Figure 2). The original experiment was carried out by WesternGECO Ltd in February 1993. Its geometric configuration is shown in Figure 3. During this experiment, a tuned array of 36 guns with a total volume of 119 liters was towed behind the vessel at an average depth of 7.5 m. Vessel speed was 2 m s^{-1} and the gun array was fired every 40 m (i.e. every 20 s). Further astern, a 4.8 km long streamer consisting of 240 hydrophones spaced every 20 m, was towed at a depth of 10 m. Horizontal offset between the airgun array and the start of the active streamer was 97 m. The common mid-point interval is 10 m which yields a 60-fold redundancy of coverage. Note that the first second of two-way travel time was not recorded during acquisition.

This dataset was previously processed and analyzed by Sheen et al. (2009). Subsequently, Holbrook et al. (2013) have shown that significantly improved seismic images can be produced by paying particular attention to elements of the processing sequence (e.g. suppression of random and harmonic noise, post-stack migration). Following Ruddick et al. (2009), Fortin and Holbrook (2009), and Holbrook et al. (2013), our refined processing methodology exploits standard techniques that are adapted from those used to construct seismic images of the solid Earth (Yilmaz 2001). There are three particularly important steps. First, band-pass and wavenumber filtering is applied to ameliorate the influence of ambient and harmonic noise, respectively. Randomly generated ambient noise is suppressed using a zero phase, band-pass (i.e. 12–100 Hz) Butterworth filter. As Holbrook et al. (2013) remark, harmonic noise can be especially significant when seismic images are spectrally analyzed in the horizontal wavenumber domain. This form of noise is shot-generated and occurs at integer multiples of the shot spacing (i.e. every 40 m or 0.025 cpm). These noise spikes are suppressed by applying a band-stop notch filter centered over each spike in the wavenumber domain.

Secondly, individual shot records are sorted into common mid-point (cmp) records which are stacked to generate a coherent seismic image with an optimal signal-to-noise ratio. Stacking is carried out by correcting for offset between each shot/receiver pair. This correction relies upon carefully choosing the root-mean-square (rms) sound speed of seawater as a function of two-way travel time for shot/receiver pairs that share a common point of reflection at depth. Although sound speed generally varies only between 1470 and 1530 m/s, these rms functions must be chosen and applied with considerable care. It is also important that velocity picking is sufficiently dense (e.g. every 1–3 km) to allow for horizontal changes in sound speed (Fortin and Holbrook 2009).

Finally, seismic data are recorded as a function of the time elapsed between generation and detection of acoustic energy (i.e. two-way travel time). To correctly locate reflected signals within the spatial domain, seismic images are migrated from elapsed time into correct depth. This migration process is carried out either before, or after, a two-dimensional seismic image is constructed by stacking. It requires knowledge of sound speed as a function of two-way travel time. Sheen et al. (2009) carried out an iterative pre-stack depth migration. However, this form of pre-stack algorithm can degrade slope spectra at higher wavenumbers (Holbrook et al. 2013). Here, we have followed the recommendations of Holbrook et al. (2013) and carried out post-stack time migration using a standard frequency-wavenumber algorithm (Stolt 1978). They also suggested that conversion to depth be carried out using a sound speed of 1500 m/s. We note that changing the sound speed used for depth conversion by $\pm$30 m/s does not significantly affect the conclusions we draw from spectral analyses.

Coeval hydrographic measurements of temperature and salinity were not acquired during this seismic experiment. Here, we have chosen a legacy hydrographic database of meter-scale resolution CTD casts acquired during December–April of 1972–2011 (`www.nodc.noaa.gov`). These casts are located less than 200 km from our seismic experiment (Figure 2a). We chose to display calculated buoyancy frequency profiles as a function of mensal range (Figure 2b-e). The average profile does not change significantly over ± 4 months (note that a subset of CTD casts, shown in Figure 2e and acquired in a single cruise, are offset to higher than expected values and are not used in our analysis). In this study, we use an average profile of N as a function of depth based upon CTD casts acquired between December and March (i.e. ± 2 months on either side of the seismic experiment). During this period, the standard deviation of the average N profile is ± 0.3 cph between 0.5 and 1.5 km.

3. Spectral Analysis of Fine Structure

a. Reflective Event Tracking

Seismic images of thermohaline fine structure reveal patterns of coherent undulating reflections. A substantial number of these reflections can be traced over distances of several kilometers (Figure 4). Although these reflections occasionally occur as transgressive filaments, they often track isopycnal surfaces (Holbrook and Fer 2005; Krahmann et al. 2008, 2009; Sheen et al. 2009; Biescas et al. 2014). This observation is sufficient, but not strictly necessary, to make inferences about the internal wavefield. A more important requirement is that, over length scales of interest, these undulations are governed by the internal wavefield. This requirement is thought to be the case when $5 \times 10^{-4} < k_x < 10^{-1}$ cpm (Krahmann et al. 2009). Most practitioners deem that it is reasonable to infer that seismic images are approximate snapshots of vertical isopycnal displacements.

In order to analyze stacked seismic images spectrally, it is necessary to track reflections (Holbrook and Fer 2005; Sheen et al. 2009). Accurate and automated tracking of discontinuous events with variable signal-to-noise ratios that variously grow, climb, descend, bifurcate, merge and die is not straightforward. Here, automated tracking was carried out using the method described by Holbrook et al. (2013). First, the amplitude of each reflection is normalized to ± 1 by calculating the cosine of the instantaneous phase angle. This angle is determined from the Hilbert transform of each individual vertical seismic trace. Secondly, the normalized reflections are contoured in order to identify and enclose individual continuous reflections. Thirdly, individual tracks are identified using the average vertical position of each contour along its length. Holbrook et al. (2013) recommend using a contour value of ± 0.6. We tested a range of values and found that a value of ± 0.8 maximizes the number of tracks, whilst still yielding faithful tracking. To remove long wavelength features that may not be generated by the internal wavefield, tracked features were linearly de-trended.

A total of 856 reflections were individually tracked across the seismic image (Figure 4b). The total length of tracked reflections on this image is 1200 km, which is broadly comparable to 880 km of tracked internal waves from a typical hydrographic experiment using a towed instrument in the vicinity of Hawaii (Klymak and Moum 2007b). Subsequently, we have chosen to analyze a sub-set of the total tracked length consisting of tracks, each of which is longer than 2 km and has a signal-to-noise ratio of greater than 3.5. These chosen values fulfil the requirement for a large range of wavenumbers and are based upon the recommendations of Holbrook et al. (2013). This sub-set has 88 tracks and a total track length of 270 km.

b. Spectra of Tracked Reflections

Power spectra of the vertical displacement of de-trended horizontal tracks were calculated using multi-taper spectral analysis. This technique produces significantly less variability and bias than a standard periodogram (Thomson 1982). Vertical displacement power spectra are converted into horizontal slope spectra using $\phi_{\zeta_x}(k_x) = (2\pi k_x)^2 \phi_\zeta(k_x)$ (Klymak and Moum 2007a). This conversion emphasises the transition from the internal wave to the turbulent regime, which now takes the form of a switch from negative to positive exponents.

We note in passing that there is little consensus on the exact value of the exponent for internal wave slope spectra which is unlikely to be constant throughout the oceanic realm. For example, the GM75 model of Garrett and Munk (1975) has an exponent of -0.5 for the internal wave slope spectrum. In contrast, the GM76 model of Cairns and Williams (1976) has an exponent of zero. Other studies suggest that a roll off occurs at an exponent of -1 toward higher wavenumbers (Gargett and Hendricks 1981). It is reasonable to infer that a range of values from 0 to -1 are consistent with slope spectra of the internal wave field. This range is qualitatively distinct from the turbulent spectrum that is expected to have an exponent of $-5/3+2=1/3$, where $+2$ comes from the multiplication by $(2\pi k_x)^2$ when converting vertical displacement spectra to slope spectra.

The suitability of a seismic image for spectral analysis is gauged by calculating its power-wavenumber spectrum (Holbrook et al. 2013). Figure 5 shows slope spectra that have been calculated for two panels of tracks shown in Figure 4. These spectra demonstrate that internal wave and turbulent regimes are present with power-law exponents of -1 and 1/3, respectively. At wavenumbers > 0.04 cpm, white noise starts to dominate and these higher wavenumbers were discarded. These spectral tests show that the turbulent regime is clearly identifiable at high wavenumbers.

Holbrook et al. (2013) emphasize the importance of identifying and removing harmonic noise which can badly contaminate slope spectra especially at higher wavenumbers. On the dataset presented here, a single harmonic noise spike occurs at $k_x = 2.5 \times 10^{-2}$ cpm which has been excised using the method described by (Holbrook et al. 2013). In Figure 6, spectral analysis of a panel from Figure 4 demonstrates that harmonic noise has been successfully removed.

c. Temporal Blurring

Finally, we tackle an issue which afflicts all hydrographic sampling technologies, namely how to adequately sample moving fluid structure. Seismic images are constructed by stacking together shot-receiver pairs which are recorded over a finite period of time. Therefore the resultant images are susceptible to blurring. This susceptibility might compromise our ability to adequately image internal wave and turbulent regimes. During stacking, multiple shot-receiver pairs (i.e. a cmp gather) that image the same portion of the sub-surface are added together (Figure 3). The time taken for a common mid-point gather to be acquired, τ, depends upon the ship's speed, V, and upon the length of the streamer, L, where

$$\tau = \frac{L}{2V}. \tag{4}$$

A finite duration of imaging will tend to blur structures which translate either vertically or horizontally by distances that are comparable to the spatial resolution of the seismic experiment. Inevitably, V is constrained by the technical requirements of towing a long streamer. However, L can effectively be changed by changing the length of streamer used during processing (i.e. discarding records from more distal portions of the streamer). A shorter streamer has a smaller imaging duration which will have the effect of sharpening the image of a moving structure at the expense of a lower signal-to-noise ratio. Conversely, a longer streamer yields an improved signal-to-noise ratio but has a greater susceptibility to blurring. In this seismic experiment, $L = 4800$ m and $V = 2$ m s^{-1} which yields $\tau \lesssim 17$ minutes. If the geostrophic velocity is 0.1 m s^{-1}, structures could move horizontally by up to 100 m during this interval. Similarly, if $N = 1$ cph, 17 minutes represents more than one quarter of the buoyancy period. In both cases, the stacked image may suffer from blurring. Thus, at the horizontal length scales of interest in this study, the vertical and horizontal motion of internal waves might, or might not, be significant compared with τ.

To estimate how spatial blurring could alter our spectral analyses, we have analyzed a series of partially stacked images which were constructed using different values of L. As L is progressively reduced from 4.8 to 1 km, τ correspondingly reduces from 17 to 3.5 minutes. The effect that decreasing values of τ have on calculated slope spectra is illustrated in Figure 7. As τ is reduced, the transition between the internal wave and turbulent regimes sharpens (compare Figure 7a and c). For $\tau \lesssim 3.5$ minutes, spectral deterioration is caused by a decrease in the signal-to-noise ratio.

This result suggests that spatial blurring is not significant at the considered timescales. An alternative, but less plausible, possibility is that blurring is always significant. We support the first possibility for two reasons. First, synthetic seismic experiments, in which τ is varied, do not significantly distort spectra. Secondly, we do not think that the clear consistency between our observed spectral power-law exponents and those measured by other hydrographic techniques is fortuitous (Klymak and Moum 2007a,b). Here, we have used $L = 4.8$ km because the signal-to-noise ratio is marginally better than for $L = 3$ km.

d. Grouped and Averaged Spectra

An important goal is identification of spectral sub-ranges from their characteristic slopes. Unfortunately, individual slope spectra have low signal-to-noise ratios and some form of preliminary averaging is desirable. First, spectra of tracked reflections $>$ 2 km in length are sorted according to their estimated energy level, which is given by the median value of each spectrum for 0.004 cpm $\leq k_x \leq 0.024$ cpm. Sorted spectra are then averaged into groups of four, yielding a total of 22 groups (Figure 8).

At low wavenumbers (i.e. $k_x < 0.002$ cpm), observed exponents are consistently negative with a pronounced roll-over at the lowest wavenumbers (i.e. a shallowing of the gradient of the reflection slope spectra). With increasing wavenumber, the steepest gradients of the slope spectra occur just before a cross-over into positive exponents. These observations are consistent with slope spectral predictions of the GM76 model which has a roll-over of up to -1 (Cairns and Williams 1976; Gargett and Hendricks 1981; Gregg 1993).

At higher wavenumbers (i.e. $k_x > 0.005$ cpm), a positive exponent of 1/3 is observed. Klymak and Moum (2007b) demonstrated that the slope spectrum of the inertial convective turbulent regime, $\phi^T_{\zeta_x}(k_x)$, is given by

$$\phi^T_{\zeta_x}(k_x) = \frac{4\pi\Gamma}{N^2} C_T \varepsilon^{2/3} (2\pi k_x)^{-5/3} (2\pi k_x)^2. \tag{5}$$

where $\Gamma = 0.2$ is the turbulent flux coefficient that relates the kinetic energy dissipation rate, ε, to an appropriately

averaged buoyancy flux (Osborn 1980). $C_T = 0.4$ is the Kolmogorov constant (Sreenivasan 1995). N is the buoyancy frequency (Equation 2).

Here, we are less concerned with the inertial diffusive sub-range where isotropic turbulence occurs at higher wavenumbers. At horizontal wavelengths that exceed 100 m, isotropic turbulence is unlikely to be the dominant process. Instead, it has been suggested that an inherently anisotropic and stratified (i.e. LAST) turbulent model applies. In this case, the horizontal kinetic energy spectrum is given by

$$E_K(k_x) = C_k \varepsilon^{2/3} k_x^{-5/3} \tag{6}$$

where k_x is horizontal wavenumber and $C_k \simeq 0.5$ is an empirical constant estimated from numerical simulations of strongly stratified turbulent fluid flow (Lindborg 2006). This model also has a power-law exponent of $-5/3$ that is equivalent to a slope spectral gradient of $1/3$.

The grouped slope spectra shown in Figure 8 suggest that internal wave and turbulent regimes are identifiable and that spectra are displaced vertically and horizontally according to energy level. However, these grouped spectra are still quite noisy and it is difficult to determine with confidence the nature of the cross-over between the two regimes. Cross-over from negative to positive gradients for slope spectra marks the transition from an internal wave regime to an appropriately defined turbulent regime. D'Asaro and Lien (2000) pointed out that the shape of this cross-over ought to contain important information about the dynamics of the transition from one regime to another (e.g. Figure 1). An additive model assumes that internal waves and layered anisotropic stratified turbulence co-exist across a range of scales whereas an onset model assumes that a significant change of behavior occurs at a cross-over scale that triggers turbulence. This turbulence is still strongly affected by stratification since this cross-over scale is assumed to be substantially larger than the Ozmidov scale l_O (*cf.* D'Asaro and Lien 2000). Thus, from a fluid dynamical perspective, an important goal is to determine the spectral shape of this cross-over. For slope spectra, the cross-over for an additive model is expected to be smooth and U-shaped without a sharply defined minimum whereas the cross-over for an onset model is expected to be sharp and V-shaped with no transitional sub-range.

Here, we address the cross-over imaging problem by calculating average normalized (i.e. stacked) spectra with a view to further improving the signal-to-noise ratios in the vicinity of the cross-over locus. Simple averaging does not faithfully preserve cross-over shape since the wavenumber at which cross-over occurs varies as a function of both energy level and stratification (Figure 10a,d,g). In order to bring the cross-over region into better focus, we have developed and tested two different forms of normalization (Figure 9). Both forms of normalization shift spectra with respect to each other. Although scaling along the x and y axes is preserved, absolute values are not. These values have been omitted from figure panels where appropriate.

Preliminary averaging into 22 groups helps to improve the signal-to-noise ratio and also allows the approximate cross-over loci to be identified on grouped spectra. For each grouped spectrum, this approximate locus is determined by fitting a three-component model with sub-ranges which have power-law exponents corresponding to internal waves, turbulence and white noise. Intersections between internal wave and turbulent sub-ranges yield a set of approximate cross-over loci. To avoid bias, those parts of the spectra within ± 0.2 logarithmic units of the predicted cross-over wavenumber are ignored when fitting the three-component model.

In linear normalization, approximate cross-over loci are fitted with a straight line using linear regression (e.g. Figure 11c). Each cross-over locus is projected orthogonally onto this line to give a projected cross-over point. Grouped spectra are then averaged in a direction that is parallel to this best-fit line (i.e. all projected cross-over points are collapsed in the direction of this line onto a single average value; Figures 10b,e,h and 11d). Thus linear normalization is equivalent to averaging parallel to a rotated y axis where the angle of rotation is that between the ϕ_{ζ_x} axis and the best-fit line. Note that linear normalization is not the same as point normalization where spectra are shifted so that the approximate cross-over loci become coincident in k_x-ϕ_{ζ_x} space.

In non-linear normalization, a value of ε is estimated from the turbulent sub-range of each grouped spectrum using Equation (5). Internal wave energy levels were then determined from values of ε using the Gregg-Henyey parametrization. Each energy level is used to calculate an internal wave spectrum for a GM76 model with a high wavenumber roll-off where $N = 1.4$ cph and $j^* = 3$ is the band-width parameter (J. Klymak, written communication, 2014; Cairns and Williams 1976; Gargett and Hendricks 1981).

Intersections between predicted internal wave and turbulent slope spectra constrain a set of cross-over points that lie along a curve in k_x-ϕ_{ζ_x} space. Normalization is achieved by sliding grouped spectra along this curve before summing and averaging (Figure 10c,f,i). In other words, averaging is carried out along a curved rather than a straight line.

Figure 10 shows the resultant spectra for simple, linear and non-linear normalization of all 22 groups of slope spectra. Note that usage of the term 'normalization' does not mean that there is a single normalization factor which relates these spectra and the original spectra. Quality of fit for all three forms of averaging with reference to the two competing models is quantitatively assessed in Figure 10d-i. When simple averaging is carried out, it is difficult to discriminate between additive and onset models. With either linear or non-linear normalization, a sharply defined cross-over location is visible which suggests that an onset model is more appropriate. It is important to emphasize that this result is not dependent on the use of multi-taper spectral analysis. Thus a method based on constructing periodograms also yields a sharp cross-over but the resultant spectra are noisier. Linear normalization is preferred since it does not require an internal wave model, apart from the choice of a representative power-law exponent. We note in passing that a sharp cross-over between internal wave and turbulent regimes has also been observed on direct data transforms of seismic images (Holbrook et al. 2013).

An important consideration is that normalization is underpinned by fitting spectra using a fixed set of sub-ranges. To address the possibility of bias, we carried out 4941 individual calculations for which power-law exponents of the internal wave and turbulent regimes were varied from -0.4 to 0.2 in 81 steps, and from -0.1 to 1.8 in 61 steps, respectively (Figure 11). As before, linear normalization was carried out to determine an average spectrum in each case. All 4941 average spectra were used to produce a density plot that shows the resulting final averaged spectrum is robust with respect to model choice (Figure 11e). This plot reinforces the observation that the transition between the internal wave and turbulent regimes is rapid and that the internal wave slope spectrum is consistent with a power-law exponent of -1 (Gargett and Hendricks 1981).

e. Monte Carlo Analysis

To further test the robustness of the normalization method, *Monte Carlo* analysis of synthetic spectra was performed. The purpose of this analysis is to address the following questions. First, can an underlying onset model be reliably recovered? Secondly, could an underlying additive model with a smooth cross-over transition be artificially sharpened to mimic an onset model? By analyzing different synthetic datasets, we can assess the robustness and reliability of both linear and non-linear normalization of spectra.

The normalization method uses a simple spectral model to identify the approximate position of the cross-over between internal wave and turbulent regimes. This procedure is necessary because normalization requires observed spectra to be translated in a direction which is compatible with all cross-over loci. It is important to ascertain whether or not this model-based translation biases the calculated average spectra in any way.

Two measures were employed to avoid artificially sharpening the cross-over region. First, when fitting the model spectrum, regions within ± 0.2 logarithmic units of the model's cross-over point were omitted. This omission prevents any single deviation from biasing cross-over location or geometry. Secondly, once the cross-over location is found, observed spectra are always normalized by translation in one direction which is either a straight line (i.e. linear normalization) or a curve (i.e. non-linear normalization). Point normalization where all cross-over locations are averaged to give a single point should be avoided.

Monte Carlo analysis was tested on a database of 88 individual synthetic spectra. These spectra were generated by adding normally distributed ($1\sigma = 0.3$) random noise to either additive or onset spectral models (Figure 12a). Cross-over loci of these synthetic spectra shift to lower wavenumbers with increasing power as expected. Consequently, a simple average of all 88 spectra will always yield an average spectrum with a smooth transition between the internal wave and turbulent regimes. As before, individual spectra were grouped according to median amplitude into 22 spectra which are shown in Figure 12b. For each group spectrum, the approximate cross-over location was found by fitting a model spectrum (Figure 12c). Group spectra were then normalized to yield an average spectrum (Figure 12d).

This procedure was repeated 500 times for different populations of random noise. The 500 calculated average spectra are summarized in the form of a density plot (Figure 12). When either an onset or an additive model is used to generate synthetic spectra, the resultant density plots show that the correct spectral shape is reliably recovered, provided that a suitable averaging procedure is applied (Figure 12e,i). The two most important features of this procedure are linear (or non-linear) normalization and omission of the central portion of grouped spectra. These features strongly mitigate against 'self-sharpening' of cross-over loci.

If central portions of spectra in the vicinity of cross-over loci are included, the expected spectral shapes are usually preserved (Figure 12f and j). If point normalization is used instead of linear normalization, spectral shapes are also largely unchanged, although a small kink is visible on the additive model (Figure 12g and h). However, if both of these features (i.e. retention of central portions and point normalization) are used, more noticeable spectral distortion can occur (Figure 12h and l). It is clear that both onset and additive spectra are artificially sharpened. The greater the value of 1σ, the more pronounced this distortion becomes.

We conclude that appropriate normalization of spectra does not cause artificial sharpening of the cross-over region. We have shown that a combination of linear normalization and omission of the central portion of spectra ensures that sharpening does not occur. It is particularly important not to use point normalization which can result in self-sharpening of spectra.

4. Fluid Dynamical Implications

Careful analysis of slope spectra from seismic images demonstrates that the turbulent regime exists to horizontal wavenumbers as low as 10^{-2} cpm. The transition from the internal wave to the turbulent regime is sharp. We wish to outline the fluid dynamical implications of these observations. Lindborg (2006) argued that a turbulent regime, exhibiting horizontal spectra with characteristic $k_x^{-5/3}$ power-law dependence at length scales which greatly exceed the Ozmidov scale, is energetically consistent with a strongly anisotropic, yet still inertial, flow regime. The existence of such a regime is supported by atmospheric and oceanographic observations with some underpinning provided by numerical simulations (Brethouwer et al. 2007; Riley and Lindborg 2008).

As already noted, this profoundly anisotropic (i.e. vertical velocities are much smaller than horizontal velocities), yet inherently three-dimensional and turbulent, flow regime is often referred to as 'stratified turbulence' in the fluid dynamical literature (Lindborg 2006; Brethouwer et al. 2007). It is characterized by the development of layering whose vertical scale is set by $l_v \sim U/N$, where U is a characteristic horizontal flow velocity. The horizontal scale, $l_h \gg l_v$, is set by the dissipation rate of turbulent kinetic energy, $l_h \sim U^3/\varepsilon$. In this case, the horizontal Froude number, F_h, is given by

$$F_h = \frac{U}{l_h N} \leq 0.02 \ll 1. \tag{7}$$

Scaling arguments suggest a relationship between l_h and the Ozmidov scale, l_O, where

$$l_h = \frac{l_O}{F_h^{3/2}} \gtrsim \frac{l_O}{0.02^{3/2}} \simeq 350 l_O. \tag{8}$$

The existence of this regime, which we refer to as the layered anisotropic stratified turbulent (LAST) regime, is supported by reinterpretation of published observations by Riley and Lindborg (2008) and of idealized numerical simulations by Brethouwer et al. (2007). Since turbulent flow within the LAST regime has a horizontal power spectrum proportional to $k_x^{-5/3}$, an associated slope spectra must have positive power-law dependence on k_x, and so, there exists a wavenumber,

k_C (i.e. length scale $l_C = 1/k_C$), at which there is a cross-over from a slope spectra with wave-like characteristics to a slope spectra with turbulent-like characteristics.

We have considered two possible cross-over models. The first is one where the observed slope spectrum is an additive combination of wave-like and turbulent-like spectra where $\phi^O_{\zeta_x} = \phi^{IW}_{\zeta_x} + \phi^T_{\zeta_x}$(Klymak and Moum 2007a,b). This additive model suggests that the wavenumber, $k_h = 1/l_h$, associated with the horizontal extent of the turbulent layers, $k_h < k_C$, (i.e. the horizontal extent of layers is larger than the cross-over scale) and that the existence of turbulence on scales smaller than l_C (i.e. wavenumbers $k > k_C$) does not immediately destroy wave-like behavior.

In this case, both turbulent and wave-like motions exist over a range of scales and the additive cross-over will be smooth and curved. The predicted flow structure, showing both wave-like motions, and turbulence patches at all horizontal scales is illustrated in Figure 13a. The inherently additive nature of the underlying power spectrum containing both wave-like and turbulence-like contributions is shown schematically in Figure 13c. This additive model is based on the observation that internal wave and turbulent spectra decay as a function of wavenumber at different rates. Therefore the cross-over scale from one power-law description to another marks the scale at which one becomes more dominant. The cross-over scale simply reflects a change in the balance of two physical processes acting over a range of scales, and the cross-over scale itself has no particular physical significance.

Due to the central scaling assumptions of the LAST regime, the vertical scale $l_v \ll l_h$ with $l_v \gg l_O$. Thus, inherently anisotropic turbulence occurs for all horizontal scales $l_O \leq l \leq l_h$. For horizontal scales smaller than l_O, stratification is, in some sense no longer sufficiently strong to affect turbulence. It is therefore possible for isotropic turbulence with a classical inertial range to occur for scales smaller than l_O provided that the Ozmidov scale is sufficiently large compared to the Kolmogorov microscale, $l_K = (\nu^3/\varepsilon)^{1/4}$, where ν is the kinematic viscosity of the fluid.

This final condition for the existence of the LAST regime (i.e. $l_O \gg l_K$) is equivalent to the requirement that the buoyancy Reynolds number, $\mathscr{R} \gg O(1)$ where

$$\mathscr{R} = \frac{\varepsilon}{\nu N^2} = \left(\frac{l_O}{l_K}\right)^{4/3}. \tag{9}$$

It is debatable what constitutes an appropriately large value of $\mathscr{R}$ for the existence of the LAST regime. Shih et al. (2005) suggest that if $\mathscr{R} > O(100)$, then the system is fully energetic (i.e. its dynamics are free of viscous effects). In contrast, Bartello and Tobias (2013) showed that a $-5/3$ spectral dependence occurs if $\mathscr{R} > O(10)$ based upon very high resolution numerical simulations.

The alternative, and our favored, onset model is illustrated in Figure 13b and d. In this case, there is a pronounced change in slope at the cross-over length scale l_C, which separates wave-like and turbulence-like spectra. At some horizontal length scale (e.g. l_h of the layers central to the LAST regime), waves break down catastrophically and practically no wave-like dynamics survive to higher wavenumbers. Wave energy is injected into the turbulent regime at this characteristic onset scale. Conversely, little turbulence exists at scales larger than the cross-over length scale. Therefore the forward cascade of turbulence ensures that the spectrum for all wavenumbers greater than the cross-over scale is completely dominated by turbulence dynamics. The slope spectrum has a $+1/3$ power-law dependence on horizontal wavenumber. This dependence is assumed to be associated with the LAST regime for $k_C = k_h < k_x < k_O$ and with classical isotropic turbulence for $k_O < k_x < k_K = 1/l_K$. Since the power-law dependence of spectra is expected to be identical both above and below the Ozmidov scale, it is reasonable to assume that any pre-multiplying factors that scale spectral power will be the same on either side of the cross-over. The predicted flow structure shows wave-like motions at large and intermediate scales but patches of turbulence at intermediate and smaller scales (Figure 13b). The inherently onset nature of the underlying power spectrum, comprising a wave-like power spectrum at low wavenumbers and a turbulence-like power spectrum at high wavenumbers, is shown schematically in Figure 13d.

For this end member, the cross-over scale has a physical meaning that corresponds to the scale at which turbulence onsets and internal waves break down. The mechanism underlying such a process is probably a scale-selective physical process that leads to a catastrophic decrease of energy within the internal wave regime. Candidate processes for such a scale-selective onset include primary internal wave instabilities and non-linear interaction within the wave field. In essence, the cross-over scale represents an injection scale for the forward cascade of turbulent energy within the LAST regime and it is reasonable to suppose that l_C corresponds to the typical horizontal scale l_h of the anisotropic and high-aspect ratio layers characteristic of this regime (Brethouwer et al. 2007). Little coherent internal wave dynamics can be expected to survive at larger wavenumbers since the wavefield breaks down due to the onset of spatially and temporally incoherent turbulent motions. Thus a sharp cross-over marks the sudden onset of stratified turbulent behavior that has limited overlap with the internal wave regime.

It is important to emphasize that the LAST regime is an idealized model for turbulence within a stratified fluid which is dynamically unaffected by rotation. The scale of the turbulent layer may be such that rotation might affect its ultimate horizontal extent. Nonetheless, the dynamics of turbulence within that layer is small enough and fast enough for rotation to be dynamically unimportant. An additional constraint is that the cross-over length scale is sufficiently small and that the flow velocities are sufficiently large so the effects of rotation can be neglected. In particular, the anisotropic turbulent layers required for the LAST regime to exist are not necessarily manifestations of the low frequency 'vortical mode' with non-zero potential vorticity affected by planetary rotation (Thorpe 2005). Finally, we note that there are alternative explanations for the existence of power spectra with a power law decay of $k_x^{-5/3}$ at wavenumbers which are inconsistent with isotropic turbulence. For example, Hua et al. (2013) suggested that baroclinic instability of pre-existing quasi-geostrophic vortices could give rise to this spectral slope. However, our observations suggest that such instability dynamics are not necessary for the manifestation of $k_x^{-5/3}$ dependence. The precise nature of the cross-over between internal wave and turbulence regimes is challenging to determine by experiment or by numerical simulation because of the required range of length and time scales. Our observations provide an important constraint.

5. Diapycnal Diffusivity

Diapycnal diffusivity, K_T, can be determined across the seismic image using slope spectra calculated from tracked reflections (Holbrook and Fer 2005; Sheen et al. 2009; Holbrook et al. 2013). First, slope spectra of all individual tracked reflections > 640 m are calculated using the methodology described in Section 3. Spectra are fitted using three power-law functions with exponents of -1, 1/3 and 2. These lines correspond to the internal wave, turbulent and white noise regimes, respectively (Figure 14). Secondly, these starting fits are only used as the basis for isolating that part of each spectrum which corresponds to turbulence. Since the power of the turbulent regime is more sensitive to energy level, we can exploit this portion of the spectra to calculate K_T. As already noted, due to the continuity that must apply between spectra associated with inertial convective isotropic turbulence below the Ozmidov scale and LAST regime turbulence above the Ozmidov scale, it is straightforward to convert $\phi^T_{\zeta_x}$ into ε using Equation (5). Following Osborn (1980), ε is converted into K_T using

$$K_T = \frac{\Gamma \varepsilon}{N^2}, \tag{10}$$

where, for simplicity, $\Gamma = 0.2$. The value of N at any depth is given by the average profile shown in Figure 2. In this way, we can determine the spatial distribution of K_T (Figure 15a). Its average value is 3.1×10^{-5} m^{2}s^{-3} which is broadly consistent with regional hydrographic studies (Garabato et al. 2004; Waterhouse et al. 2014). The spatial variation of K_T closely follows the geometry of the thermohaline structure. For example, reduced values of K_T occur over an eddy structure located at a range of 70 km and at a depth of 900 m. Bands of changing values of K_T cross-cut the image, dipping in the opposite direction to the bathymetric slope. The apparent increase in K_T toward the sea surface is probably an artifact caused by an increase in ambient noise. We note in passing that Sheen et al. (2009) carried out similar mixing calculations based on spectral analysis of both internal wave and turbulent regimes. However, a direct data transform analysis of their processed image highlighted the drawbacks of their particular implementation of a frequency-wavenumber migration algorithm (Holbrook et al. 2013). Furthermore, Sheen et al. (2009) used a less robust form of reflection tracking that introduced spectral artifacts, especially at $k_x > 10^{-2}$ m^{-1}. Consequently, Figure 2b of Sheen et al. (2009) differs in several respects from Figure 15b.

Values of ε and N can be used to calculate the variation of Ozmidov lengthscale, l_O, across the image using Equation (1). We obtain l_O values of $O(0.1\text{–}1 \text{ m})$, which agree with those previously observed (e.g. Gargett and Hendricks 1981). These values are substantially smaller than the length scales at which the spectral characteristics of turbulence (i.e. $k_x^{-5/3}$) are observed.

Previous analyses of seismic reflection images exploited both internal wave and turbulent regimes to constrain dissipation, and hence diapycnal diffusivity, using the Osborn (1980) model. These approaches assumed a power-law exponent of -0.5 for the internal wave slope spectrum, in accordance with the GM75 model (Garrett and Munk 1975). However, competing models for the exponent of the internal wave slope spectrum exists and values between 0 to -1 could reasonably be used. An attractive property of the onset model is that diffusivity calculations are independent of the slope chosen for the internal wave regime. To compare onset and additive values of K_T, we chose a value of -0.5 for the exponent of the internal wave regime in agreement with the GM75 model and with previous seismic oceanographic studies (Holbrook and Fer 2005; Krahmann et al. 2008; Sheen et al. 2009; Holbrook et al. 2013).

An onset model necessarily yields higher estimates for K_T. This outcome occurs for purely geometric reasons since, for a given value of K_T, an additive spectrum will always have higher amplitude than an onset spectrum. Hence when fitting slope spectral data, a lower K_T will be required to match the amplitudes observed in the input data if the additive model is used. In areas where the signal-to-noise ratio is ≥ 4, the average increase in the value of K_T is by a factor of ~ 2 with considerable spatial variation. Note that we do not calculate K_T from the internal wave regime. Instead, we assume that this regime is well represented by a single power-law relationship. We then use either an additive or an onset model in the fitting stage. K_T is calculated from the turbulent component alone. This procedure sidesteps the vexed issue of equating K_T with power of the internal wave regime.

The fact that similar reflections are sometimes located above and below one another means that individual undulations are not statistically independent. This possibility could affect uncertainties at lower wavenumbers but a detailed study is beyond the scope of this study. Calculated mixing rates, which rely on the higher wavenumber portion of spectra, are unlikely to be adversely affected by a lack of statistical independence. Other sources of uncertainty can be estimated and their effects propagated using Equations 5 and 10. For example, Γ and C_T have uncertainties of at least ± 0.04 and ± 0.05 which yield uncertainties in $\log_{10} K_T$ of ± 0.04 and ± 0.08 logarithmic units (i.e. $\sim 9\%$ and $\sim 20\%$), respectively (Moum 1996; Sreenivasan 1995). Note that the likely uncertainty in the sound speed profile used for depth conversion yields a small shift in K_T of $\sim \pm 0.025$ logarithmic units (i.e. $\sim 5\%$).

N is probably the most important source of uncertainty in this study, particularly since coeval hydrographic measurements are unavailable (Figure 2). The mean value of N observed between

500 and 1500 m depth and within ± 2 months of the survey month is 1.32 cph with a standard deviation of $\sigma = 0.3$. Over 90% of N measurements fall between 0.5 cph and 2.5 cph. If $N \pm 1\sigma$ is propagated through Equations (5) and (10), the resulting $\log_{10} K_T$ for a given ε changes by about -0.5 and $+0.3$ logarithmic units (i.e. a decrease of 70% or an increase of 100%), respectively. (compare Figure 15b, c and d). This uncertainty in K_T is small compared to the observed spatial variation of K_T. Furthermore, since legacy buoyancy frequency profiles tend to have similar shapes but different magnitudes, it is likely that this uncertainty yields a static shift away from the correct values rather than variable spatial patterns. An important *caveat* exists for regions where thermohaline structures manifest horizontal variability. For example, the region above the eddy in Figure 15 may have lower rates of mixing. If so, higher stratification (i.e. $N \approx 5$ cph) caused by vertical compression of isopycnal surfaces could account for this observation. If the observed variation in $\phi^T_{\zeta_x}$ is solely caused by buoyancy frequency changes and if ε is fixed at 10^{-10} m^2 s^{-3}, N would have to vary between 0.5 and 7 cph which is a larger range than hydrographic observations could reasonably support (Figure 16).

One final source of uncertainty arises from fitting noisy spectra. In Figure 14b-d, the identified turbulent sub-range is fitted by systematically varying K_T. In each case, the misfit, χ^2, is plotted as a function of K_T. Well-defined global minima exist and, for an appropriate tolerance (e.g. twice the minimum value of χ^2), the uncertainty in K_T is no worse than one half of an order of magnitude. The uncertainty that arises from actual identification of the turbulent sub-range, which we believe to be robust, is beyond the scope of this contribution. It is important to emphasize that all of these sources of uncertainty do not affect our two principal conclusions. First, the lowest wavenumber portion of the -5/3 sub-range cannot be accounted for by isotropic (i.e. Kolmogorov) turbulence but are consistent with the layered anisotropic stratified turbulent (LAST) model (Lindborg 2006). Secondly, a sharp onset cross-over between internal wave and turbulent regimes exists.

6. Conclusions

We show that horizontal slope spectra obtained by tracking reflections across a two-dimensional seismic image have the expected power-law relationships. The high quality of these data, combined with auto-tracking methodology and spectral analysis, permit closer investigation of the cross-over from internal wave to turbulent regimes for vertical displacement power spectra. This cross-over occurs at horizontal length scales that are substantially larger than that those considered plausible for isotropic turbulence. Instead, it is more likely that cross-over is caused by the onset of a flow regime that we have referred to as the layered anisotropic stratified turbulent (LAST) regime.

Our results suggest that cross-over between regimes is rapid. In particular, we do not observe a transitional sub-range that would be characteristic of an additive model in which internal waves and turbulence co-exist over a range of scales. This observation suggests that there is a switch in the governing fluid dynamics from internal waves to turbulence without a significant overlap of the two regimes. A sharp transition is suggestive of an instability or non-linear process that causes the internal wavefield to break down catastrophically so that little energy remains within the wavefield at smaller scales. This breakdown to the LAST regime occurs at a well-defined length scale which is substantially larger than the Ozmidov scale. Central to our interpretation is the existence of a scale-selective mechanism which destroys the wavefield and sets the characteristic large injection scale of the turbulent dynamics. It remains a challenge to identify this mechanism.

Acknowledgments. M.F. is supported by the Department of Earth Sciences. Research activity of C.P.C. is supported by EPSRC Programme Grant EP/K034529/1 ("Mathematical Underpinnings of Stratified Turbulence"). We thank C. Bond, A. Dickinson, K. Gunn, S. Holbrook, J. Klymak, J. Moum and S. Thorpe for their help. We are very grateful to J. Klymak for generously making available his MATLAB toolbox for calculating Garrett-Munk spectra. Department of Earth Sciences contribution number esc.XXXX.

References

Bartello, P., and S. M. Tobias, 2013: Sensitivity of stratified turbulence to the buoyancy Reynolds number. *J. Fluid Mech.*, **725**, 1–22, doi:10.1017/jfm.2013.170.

Batchelor, G. K., I. D. Howells, and A. A. Townsend, 1959: Small-scale variation of convected quantities like temperature in turbulent fluid Part 2. The case of large conductivity. *J. Fluid Mech.*, **5**, doi:10.1017/S0022112059000106.

Biescas, B., B. R. Ruddick, M. R. Nedimovic, V. Sallarès, G. Bornstein, J. F. Mojica, and A. C. Dave, 2014: Recovery of temperature, salinity, and potential density from ocean reflectivity. *J. Geophys. Res. Ocean.*, **119 (5)**, 3171–3184, doi:10.1002/jgrc.20224.

Brethouwer, G., P. Billant, E. Lindborg, and J.-M. Chomaz, 2007: Scaling analysis and simulation of strongly stratified turbulent flows. *J. Fluid Mech.*, **585**, 343–368, doi:10.1017/S0022112007006854.

Cairns, J. L., and G. O. Williams, 1976: Internal Wave Observations From a Midwater Float, 2. *J. Geophys. Res.*, **81 (12)**, 1943–1950.

Corrsin, S., 1951: On the Spectrum of Isotropic Temperature Fluctuations in an Isotropic Turbulence. *J. Appl. Phys.*, **22 (4)**, 469–473, doi:10.1063/1.1699986.

D'Asaro, E. a., and R.-C. Lien, 2000: The Wave Turbulence Transition for Stratified Flows. *J. Phys. Oceanogr.*, **30 (7)**, 1669–1678, doi:10.1175/1520-0485(2000)030⟨1669:TWTTFS⟩2.0.CO;2.

Fortin, W. F. J., and W. S. Holbrook, 2009: Sound speed requirements for optimal imaging of seismic oceanography data. *Geophys. Res. Lett.*, **36 (April)**, 1–4, doi:10.1029/2009GL038991.

Garabato, A. C. N., K. L. Polzin, B. A. King, K. J. Heywood, and M. Visbeck, 2004: Widespread intense turbulent mixing in the Southern Ocean. *Science*, **303 (5655)**, 210–213, doi:10.1126/science.1090929.

Gargett, A., and P. Hendricks, 1981: A composite spectrum of vertical shear in the upper ocean. *J. Phys. Oceanogr.*, **11 (9)**, 1258–1271.

Garrett, C., and W. Munk, 1975: Space-Time of Internal Waves. *J. Geophys. Res.*, **80 (3)**, 291–297.

Gregg, M. C., 1993: Varieties of fully resolved spectra of vertical shear. *J. Phys. Oceanogr.*, **23 (1)**, 124–141.

Holbrook, W. S., and I. Fer, 2005: Ocean internal wave spectra inferred from seismic reflection transects. *Geophys. Res. Lett.*, **32 (15)**, L15 604, doi:10.1029/2005GL023733.

Holbrook, W. S., I. Fer, R. W. Schmitt, D. Lizarralde, J. M. Klymak, L. C. Helfrich, and R. Kubichek, 2013: Estimating Oceanic Turbulence Dissipation from Seismic Images. *J. Atmos. Ocean. Technol.*, **30 (8)**, 1767–1788, doi:10.1175/JTECH-D-12-00140.1.

Holbrook, W. S., P. Páramo, S. Pearse, and R. W. Schmitt, 2003: Thermohaline fine structure in an oceanographic front from seismic reflection profiling. *Science*, **301**, 821–824, doi:10.1126/science.1085116.

Hua, B. L., C. Ménesguen, S. Le Gentil, R. Schopp, B. Marsset, and H. Aiki, 2013: Layering and turbulence surrounding an anticyclonic oceanic vortex: in situ observations and quasi-geostrophic numerical simulations. *J. Fluid Mech.*, **731**, 418–442, doi:10.1017/jfm.2013.369.

Klymak, J. M., and J. N. Moum, 2007a: Oceanic Isopycnal Slope Spectra. Part I: Internal Waves. *J. Phys. Oceanogr.*, **37 (5)**, 1215–1231, doi:10.1175/JPO3073.1.

Klymak, J. M., and J. N. Moum, 2007b: Oceanic Isopycnal Slope Spectra. Part II: Turbulence. *J. Phys. Oceanogr.*, **37 (5)**, 1232–1245, doi:10.1175/JPO3074.1.

Kolmogorov, A., 1941: Dissipation of energy in locally isotropic turbulence. *Dokl. Akad. Nauk SSSR*, **32 (1)**, 16–18.

Krahmann, G., P. Brandt, D. Klaeschen, and T. Reston, 2008: Mid-depth internal wave energy off the Iberian Peninsula estimated from seismic reflection data. *J. Geophys. Res.*, **113 (C12)**, 1–12, doi:10.1029/2007JC004678.

Krahmann, G., C. Papenberg, P. Brandt, and M. Vogt, 2009: Evaluation of seismic reflector slopes with a Yoyo-CTD. *Geophys. Res. Lett.*, **36**, 1–5, doi:10.1029/2009GL038964.

Lindborg, E., 2006: The energy cascade in a strongly stratified fluid. *J. Fluid Mech.*, **550**, 207–241, doi:10.1017/S0022112005008128.

Moum, J. N., 1996: Efficiency of mixing in the main thermocline. *J. Geophys. Res.*, **101**, doi:10.1029/96JC00508.

Nandi, P., W. S. Holbrook, S. Pearse, P. Páramo, and R. W. Schmitt, 2004: Seismic reflection imaging of water mass boundaries in the Norwegian Sea. *Geophys. Res. Lett.*, **31 (23)**, doi:10.1029/2004GL021325.

Obukhov, A., 1949: Structure of the temperature field in turbulent flow. *Izv. Akad. Nauk SSSR, Ser. Geofiz*, **13**, 58–69.

Osborn, T. R., 1980: Estimates of the Local Rate of Vertical Diffusion from Dissipation Measurements. *J. Phys. Oceanogr.*, **10**, 83–89, doi:10.1175/1520-0485(1980)010⟨0083:EOTLRO⟩2.0.CO;2.

Riley, J. J., and E. Lindborg, 2008: Stratified Turbulence: A Possible Interpretation of Some Geophysical Turbulence Measurements. *J. Atmos. Sci.*, **65 (7)**, 2416–2424, doi:10.1175/2007JAS2455.1.

Riley, J. J., and E. Lindborg, 2010: *Chapter 7 - Recent Progress in Stratified Turbulence*. Cambridge University Press, Cambridge, 437 pp.

Ruddick, B. B. B., H. Song, and C. Dong, 2009: Water column seismic images as maps of temperature gradient. *Oceanography*.

Sallarès, V., B. Biescas, G. G. Buffett, R. Carbonell, J. J. Dañobeitia, and J. L. Pelegrí, 2009: Relative contribution of temperature and salinity to ocean acoustic reflectivity. *Geophys. Res. Lett.*, **36 (20)**, 1–6, doi:10.1029/2009GL040187.

Sheen, K. L., N. J. White, and R. W. Hobbs, 2009: Estimating mixing rates from seismic images of oceanic structure. *Geophys. Res. Lett.*, **36**, 2–6, doi:10.1029/2009GL040106.

Shih, L. H., J. R. Koseff, G. N. Ivey, and J. H. Ferziger, 2005: Parameterization of turbulent fluxes and scales using homogeneous sheared stably stratified turbulence simulations. *J. Fluid Mech.*, **525**, 193–214, doi:10.1017/S0022112004002587.

Sreenivasan, K., 1995: On the universality of the Kolmogorov constant. *Phys. Fluids*, **7 (11)**, 2778–2784.

Stolt, R. H., 1978: Migration by Fourier Transform. *Geophysics*, **43 (1)**.

Thomson, D., 1982: Spectrum estimation and harmonic analysis. *Proc. IEEE*, **70 (9)**, 1055–1096.

Thorpe, S. A., 2005: *The Turbulent Ocean*. Cambridge University Press, 439 pp.

Waterhouse, A. F., and Coauthors, 2014: Global Patterns of Diapycnal Mixing from Measurements of the Turbulent Dissipation Rate. *J. Phys. Oceanogr.*, **44 (7)**, 1854–1872, doi: 10.1175/JPO-D-13-0104.1.

Yilmaz, O., 2001: *Seismic Data Analysis*. Society of Exploration Geophysicists, 2027 pp.

LIST OF TABLES

Symbol	Description	Value	Unit	Dimension
L	Length of streamer		m	L
τ	Imaging duration		min	T
V	Ship speed	2	m s^{-1}	L T^{-1}
l_o	Ozmidov length		m	L
ε	Dissipation rate		m^2 s^{-3}	L^2 T^{-3}
N	Buoyancy frequency		cph	T^{-1}
k_x	Horizontal wavenumber		m^{-1}	L^{-1}
ϕ_ζ	Horizontal vertical displacement spectrum		cpm^{-3}	L
ϕ_{ζ_x}	Horizontal slope spectrum		cpm^{-1}	L
E_K	Horizontal kinetic energy spectrum		m^3 s^{-2}	L^3 T^{-2}
Γ	Dissipation flux coefficient	0.2		
C_T	Kolmogorov constant	0.4		
g	Gravitational acceleration	9.81	m s^{-2}	L T^{-2}
ρ	Potential density		kg m^{-3}	M L^{-3}
K_T	Thermal diffusivity		m^2 s^{-1}	L^2 T^{-1}
F_h	Froude number			
U	Characteristic velocity		m s^{-1}	L T^{-1}
l_h	Characteristic horizontal lengthscale		m	L
l_v	Characteristic vertical lengthscale		m	L
l_c	Characteristic lengthscale of crossover		m	L
$\mathscr{R}$	Buoyancy Reynolds number			
ν	Kinematic viscosity		m^2 s^{-1}	L^2 T^{-1}

TABLE 1. Constants and variables

LIST OF FIGURES

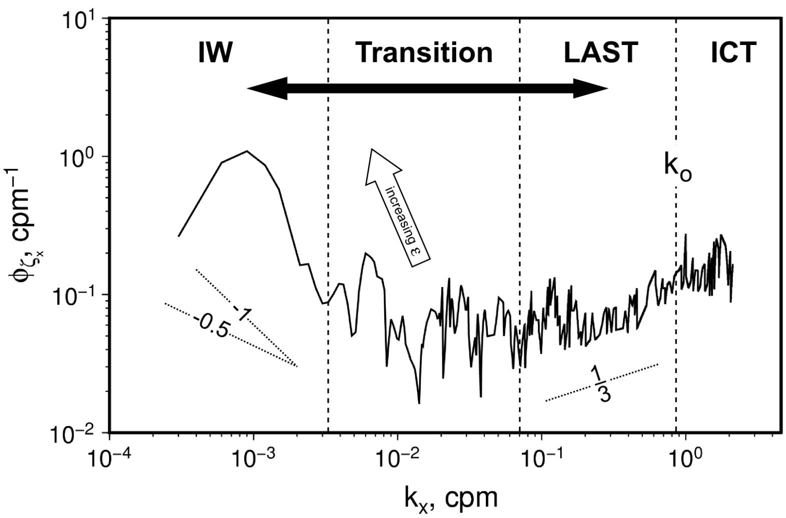

812 FIG. 1. General form of observed spectra illustrated by example from Klymak and Moum (2007a). IW/LAST/ICT = Internal Wave, Layered Anisotropic Stratified Turbulent, and Inertial Convective Turbulent regimes; k_O = Ozmidov wavenumber (i.e. $1/l_O$); solid arrow = length scales observed on seismic images; open arrow = direction of migration of transition from internal wave to turbulent regime with increasing ε. Labelled guidelines have gradients of $\frac{1}{3}$, -1 and -0.5.

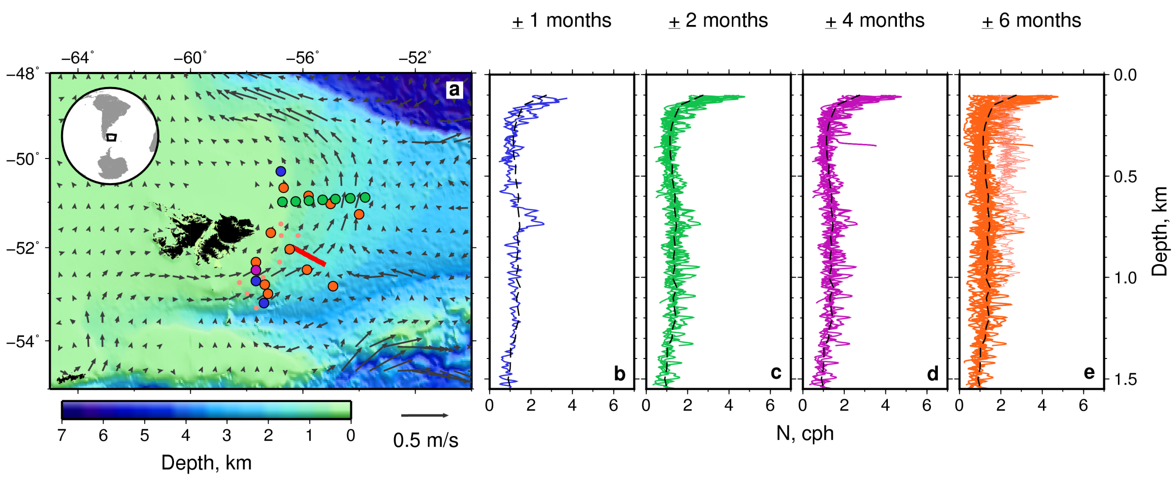

FIG. 2. (a) Bathymetric map of region encompassing Falkland Islands (see inset). Red line = seismic reflection profile acquired by WesternGECO Ltd. in February 1993; colored circles = loci of legacy CTD casts that are plotted smoothed by a 25 m Gaussian window, and colored according to mensal range; black arrows = geostrophic velocity field from exact day of seismic experiment determined from satellite altimetric data. (b-e) Buoyancy frequency, N, as function of depth calculated from legacy CTD casts for mensal range straddling February (blue = $\pm$1 month; green = $\pm$2 months; purple = $\pm$4 months; orange = $\pm$6 months; pale orange = set of outlying CTD casts acquired on *Capitano Cabalda* in September 1994). In each case, dashed black lines = average profile calculated using 50 m Gaussian window for $\pm$2 months used in this study. Altimetric products produced by Ssalto/Duacs and distributed by Aviso with support from Cnes.

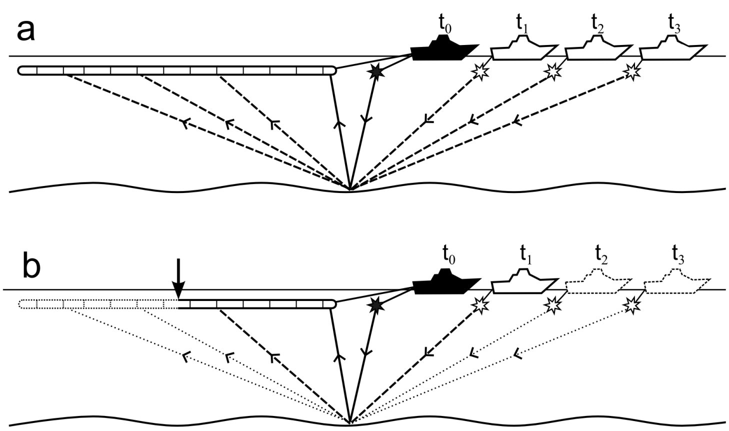

FIG. 3. Set of cartoons showing evolving geometry of seismic reflection experiment. (a) Solid black ship = locus of vessel at time t_0; open ships = loci of vessel at subsequent times t_1, t_2 and t_3; horizontal band with vertical lines = 4.8 km long streamer with 240 receiver groups; undulating line = moving reflector within water column; stars with solid/dashed lines and arrows = successive acoustic shots and associated ray paths. Each locus on sub-surface reflector is sampled by many different shot/receiver pairs over period of time governed by speed of vessel, V, and length of streamer, L. (b) Reduced streamer length where dotted ships, streamer and ray paths identify those shot-receiver pairs that have been omitted. Vertical arrow = reduced streamer length. Streamer is only shown at time t_0 for clarity.

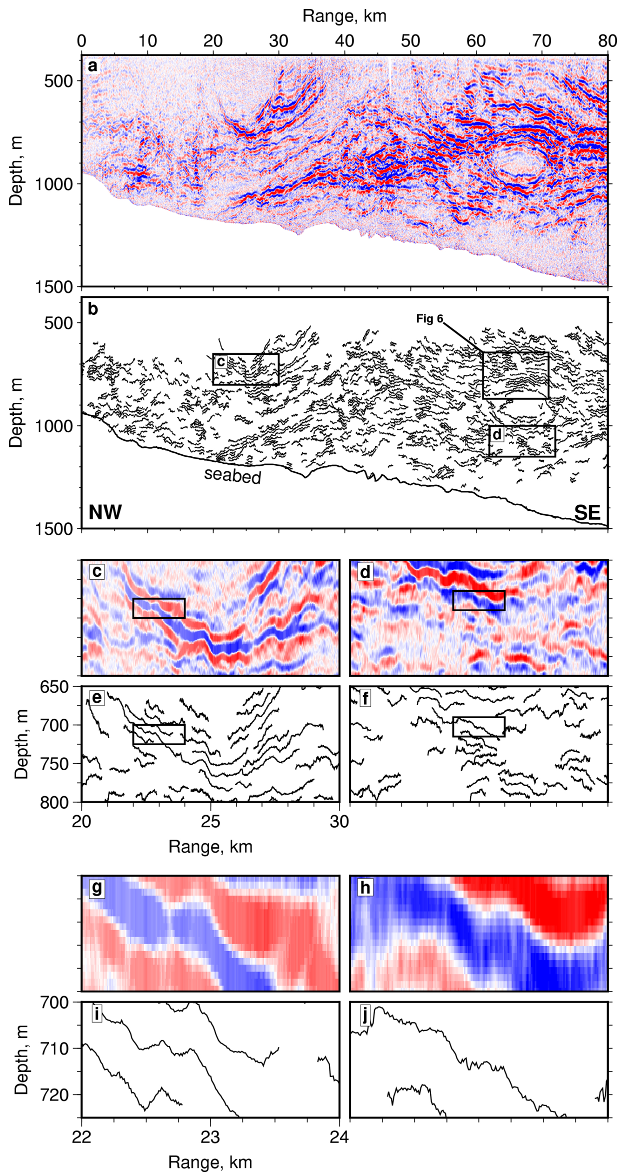

834 FIG. 4. (a) Seismic reflection profile (see Figure 2 for location). Red/blue stripes = reflections of positive and negative polarity within water column; irregular sloping base = sea bed. (b) Automatically tracked reflections. Labelled boxes are shown in (c) and (d) and in Figure 6. (c) and (d) 10 km × 150 m zoomed panels located in (b). (e) and (f) automatically tracked reflections. (g) and (h) 2 km × 25 m zoomed panels located in (e) and (f). (i) and (j) automatically tracked reflections.

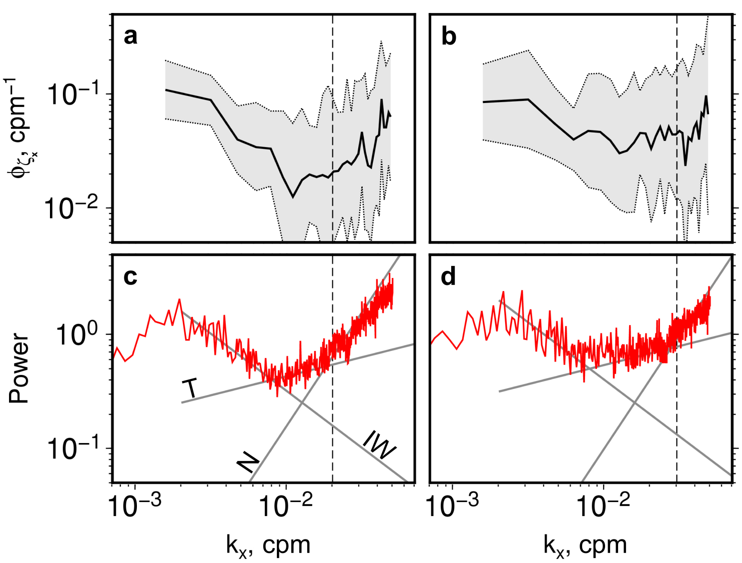

FIG. 5. (a) Slope spectrum, ϕ_{ζ_x}, plotted as function of horizontal wavenumber, k_x, for tracked reflections shown in panel (e) of Figure 4. Solid/dotted lines and gray band = average/standard deviation. (b) As before for panel (f) of Figure 4. (c) Direct data transform of tracked reflections shown in panel (e) of Figure 4 and plotted as function of horizontal wavenumber, k_x (see Holbrook et al. (2013)). Red line = direct data transform; gray lines labelled IW, T, and N = expected slopes for internal wave (-1), turbulent ($1/3$), and ambient noise regimes (2); dashed line = onset of ambient noise regime. (d) As before for panel (f) of Figure 4.

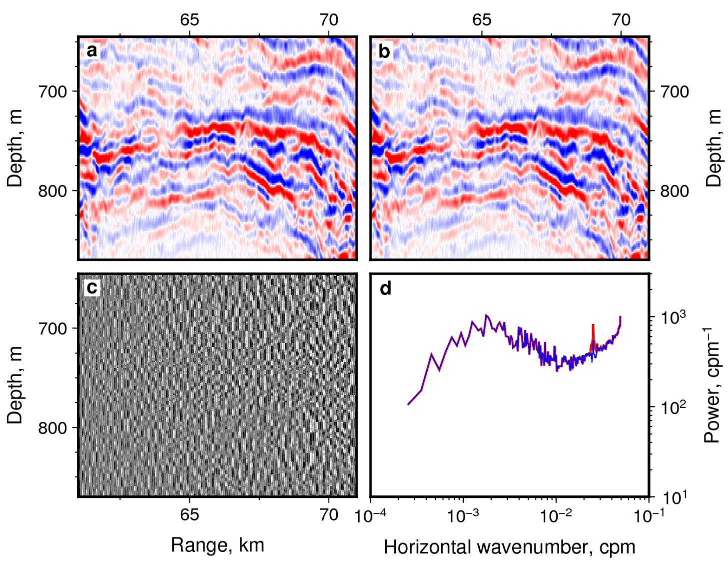

FIG. 6. (a) Zoomed panel of original seismic reflection profile (see Figure 4b for location). (b) Same panel after harmonic noise has been removed using k_x notch filter described by Holbrook et al. (2013). (c) Difference between panels (a) and (b) which shows harmonic noise removed by filtering. (d) Slope spectra calculated directly from seismic images. Red line = slope spectrum for panel (a); blue line = slope spectrum for panel (b). Note removal of harmonic noise spike at $k_x = 2.5 \times 10^{-2}$ cpm.

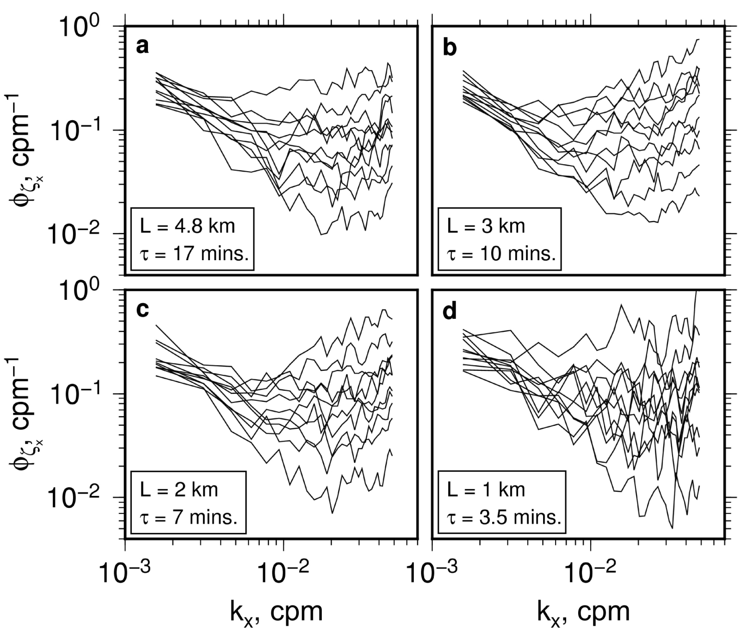

850 FIG. 7. Vertical displacement slope spectra plotted as function of k_x (sorted by median amplitude, binned into
851 11 groups, geometrically smoothed). Reflection tracks > 1.5 km were used. (a) Streamer length is $L = 4.8$ km,
852 imaging duration is $\tau = 17$ minutes. (b) $L = 3$ km, $\tau = 10$ minutes. (c) $L = 2$ km, $\tau = 7$ minutes. (d) $L = 1$ km,
853 $\tau = 3.5$ minutes.

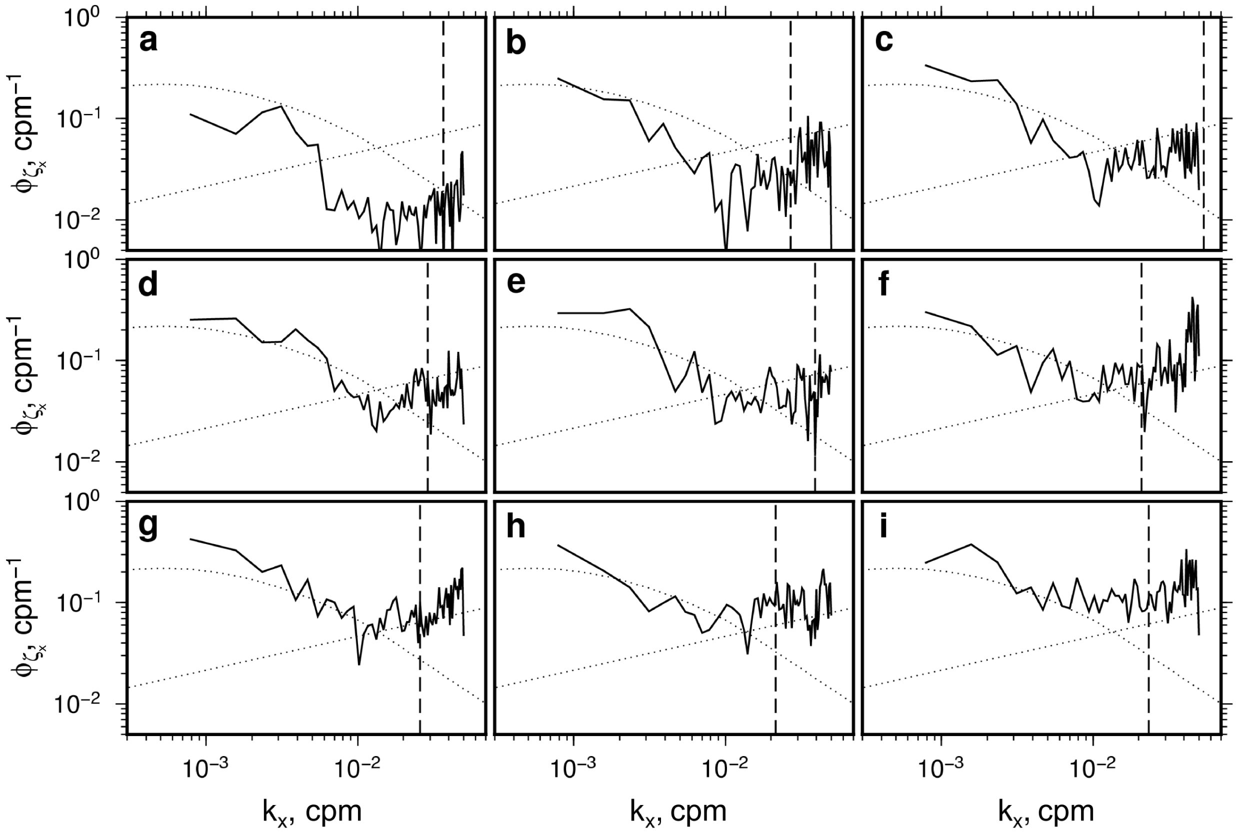

854 FIG. 8. (a)–(i) 9 of 22 total grouped slope spectra (see text for explanation). Spectral power, ϕ_{ζ_x}, plotted as function of horizontal wavenumber, k_x. Black lines = average slope spectrum calculated for four tracked reflections; dotted lines = Garrett-Munk spectrum ($j^\star = 3$, E/E$_{GM}$ = 2.5) and turbulent spectrum for equivalent value of ε, calculated using the Gregg-Henyey method. Note these are not fits but visual references that are identical in each panel. Vertical dashed line = ambient noise regime.

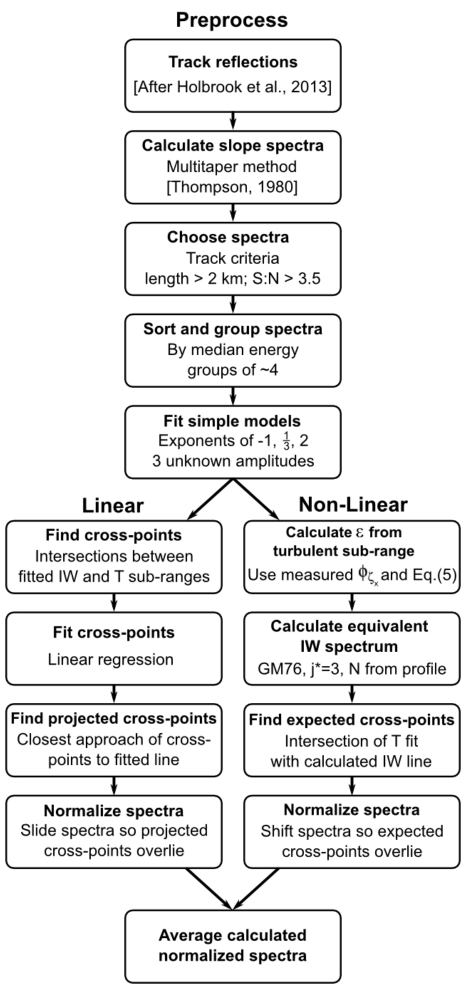

FIG. 9. Flow diagram illustrating linear and non-linear normalized averaging methodology.

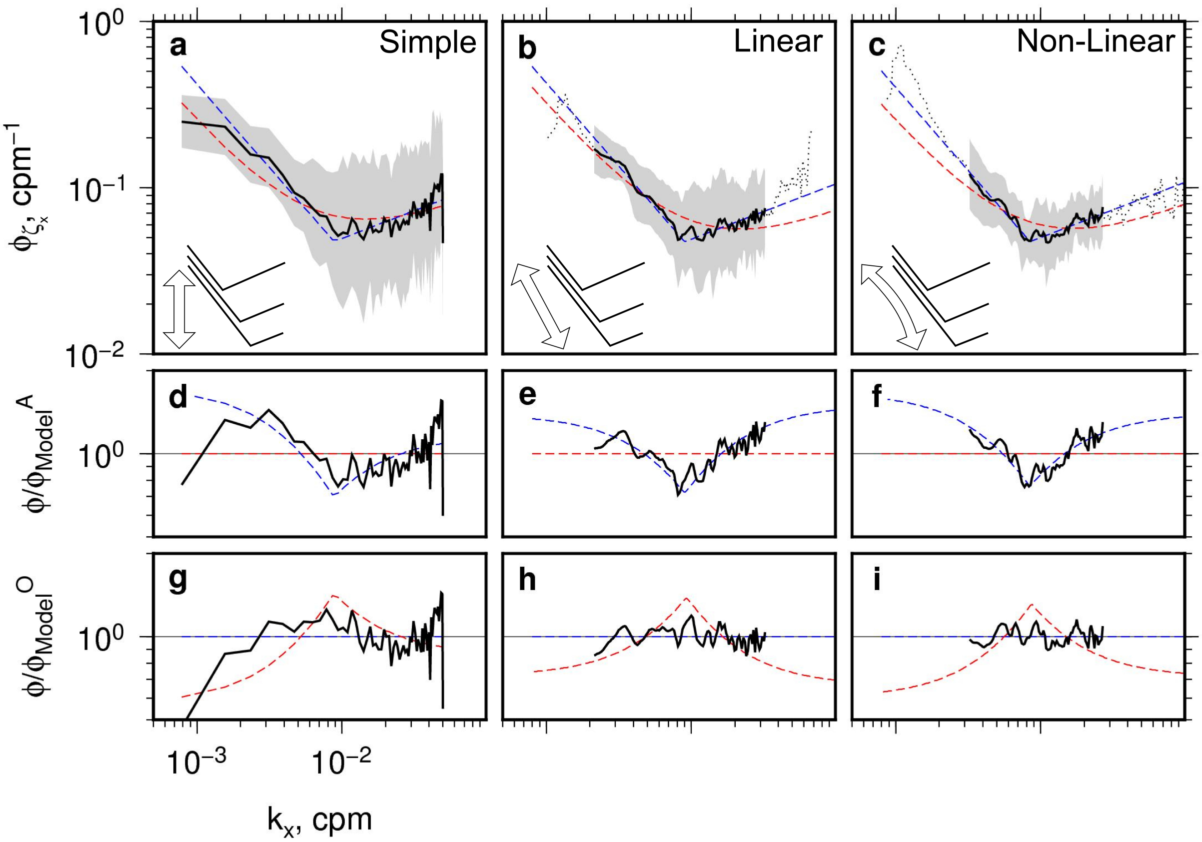

FIG. 10. Analyses of transition from internal wave to turbulent regime. (a) Simple (i.e. vertical) averaging. Black line = average spectrum where all 22 grouped spectra contribute (see text); dotted line = average spectrum where fewer than 22 grouped spectra contribute ; red dashed line = best-fit additive model; blue dashed line = best-fit onset model; cartoon in bottom left-hand corner shows mode of averaging. (d) Average spectrum divided by additive model. (g) Average spectrum divided by onset model. (b), (e) and (h) Averaging post linear normalization. (c), (f) and (i) Averaging post non-linear normalization. Normalization means that absolute numerical values along axes have no meaning and are omitted as necessary.

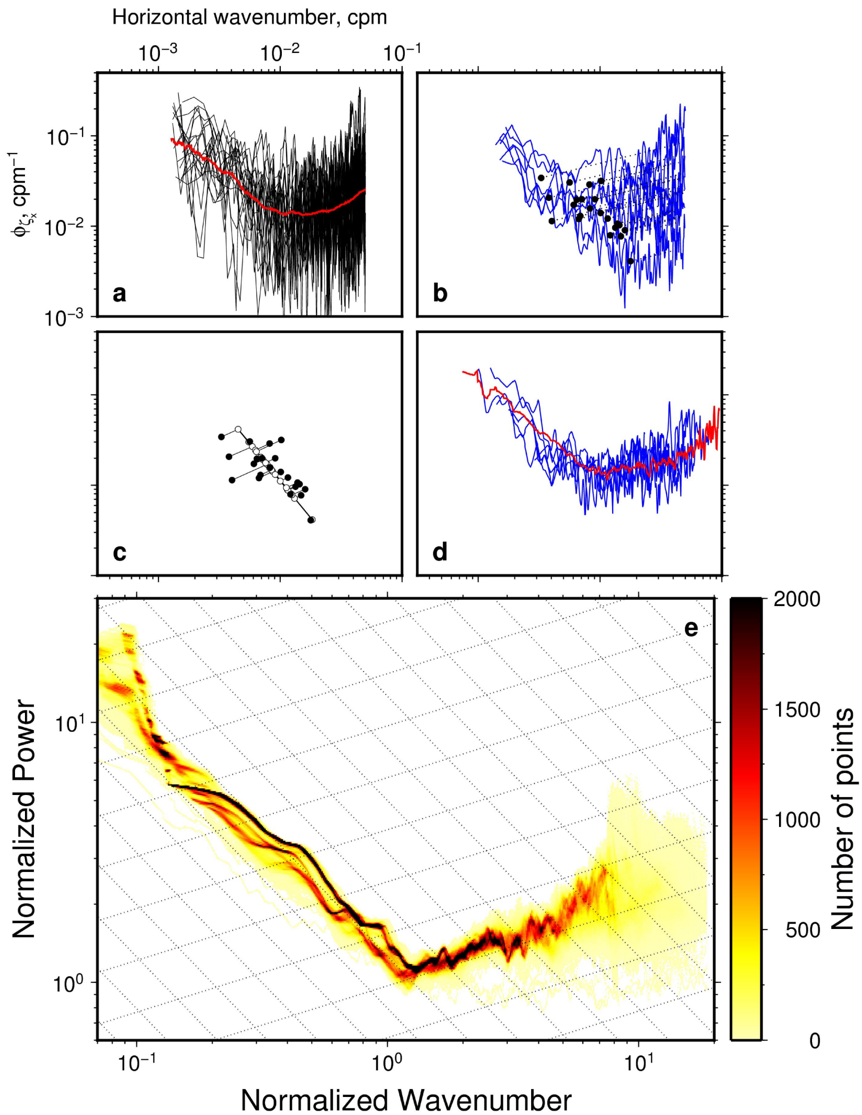

FIG. 11. Analysis of averaged spectra. (a) Black lines = 22 of 88 individual spectra determined from tracked reflections; red line = simple average spectrum. (b) Blue lines = 11 of 22 grouped spectra; solid circles = crossover loci identified by model fitting (± 0.2 log units of each crossover locus ignored); dotted lines on right-hand side = fits for turbulent regime. (c) Solid circles = crossover loci; open circles = loci projected onto linear relationship. (d) Blue lines = normalized grouped spectra calculated by collapsing open circles shown in panel (c) to single point along linear relationship; red line = average spectrum. (e) Density plot of linear averaged and normalized spectra where large range of spectral models was used to identify crossover loci shown in panel (c). Gradient of internal wave regime varied between -0.4 and -2 with steps of 0.2; gradient of turbulent regime varied between ~ 0.1 and ~ 1.8 with steps of 0.03; fine dotted reticule indicates slopes of -1 and $1/3$. Normalization means that absolute numerical values along axes have no meaning and are omitted as necessary.

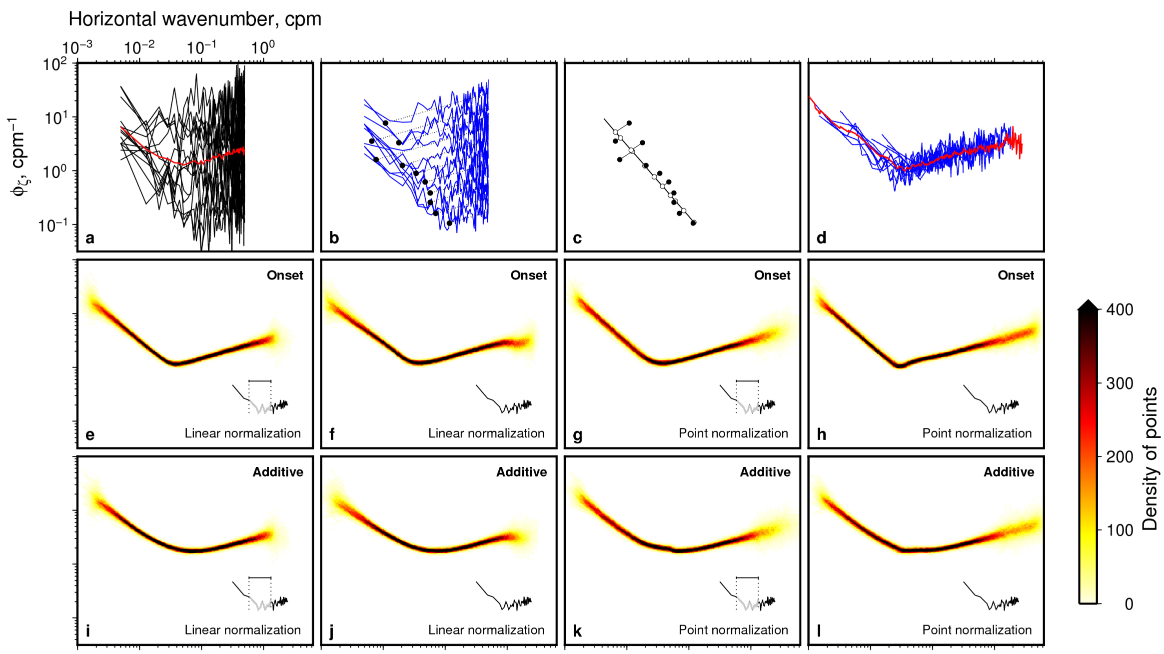

FIG. 12. *Monte Carlo* analysis of synthetic spectra. (a) Black lines = 22 of 88 synthetic spectra generated by adding normally distributed random noise to known model where $1\sigma = 0.3$ log units; red line = simple average spectrum. (b) Blue lines = 11 of 22 grouped spectra; solid circles = crossover loci identified by model fitting (± 0.2 log units of each crossover locus ignored); dotted lines on right-hand side = fits for turbulent regime. (c) Solid circles = crossover loci; open circles = loci projected onto linear relationship. (d) Blue lines = normalized grouped spectra calculated by collapsing open circles shown in panel (c) onto single point along linear relationship; red line = average spectrum. (e) Density plot of linear averaged and normalized spectra for 500 synthetic onset datasets using approach described in Figure 11. Central gray portion of spectrum at bottom right-hand side highlights portion of spectra within ± 0.2 log units of crossover locus omitted for model fitting stage. (f) Density plot as in (e) where complete spectrum is used. (g) Density plot of point averaged and normalized spectra constructed from central portion of spectra. (h) Density plot as in (g) where complete spectrum is used. (i)-(l) Equivalent set of density plots for 500 synthetic additive datasets. Black arrows in (h,k,l) indicate artifacts introduced by the point normalization method. Normalization means that absolute numerical values along axes have no meaning and are omitted as necessary.

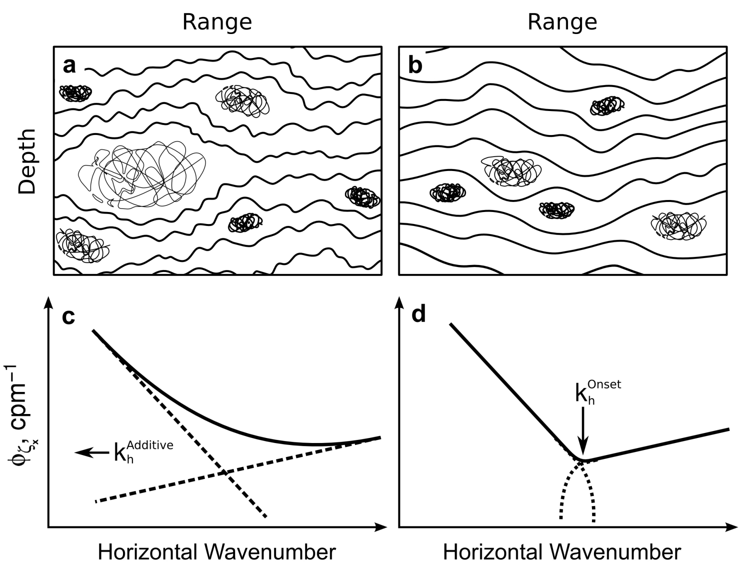

890 FIG. 13. Sketches illustrating end-member mixing models and their spectra. (a) Additive model where internal wave and turbulent regimes significantly overlap. (b) Onset model where internal and turbulent regimes do not overlap but disappear at different critical length scales. (c) and (d) schematic slope spectra for additive and onset models, respectively. k_h = low-wavenumber extent of LAST sub-range (for onset model, k_h equates to crossover locus; for additive model, k_h must extend to lower wavenumbers.

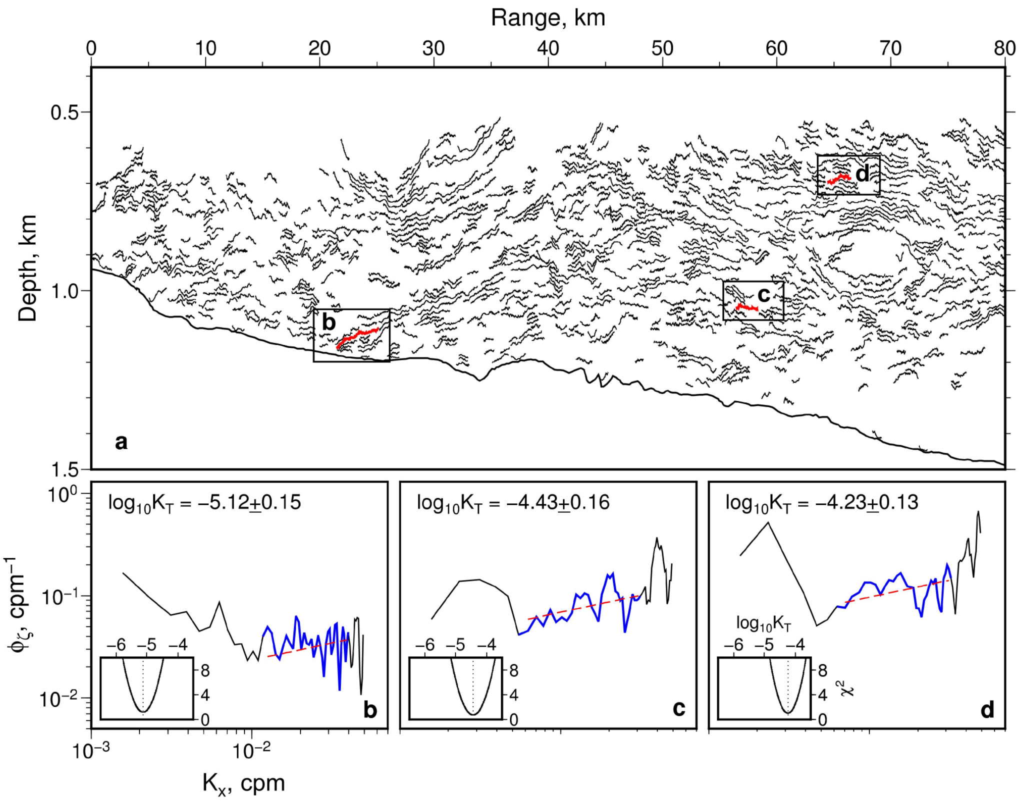

FIG. 14. (a) Automated tracking of seismic profile (Figure 4a). Red tracked reflections inside boxes are spectrally analyzed in (b)-(d). (b) Black/blue line = slope spectrum for tracked reflection with identified turbulent regime shown in blue; red dashed line = best-fit model to turbulent regime; inset = residual misfit, χ^2 as function of K_T.

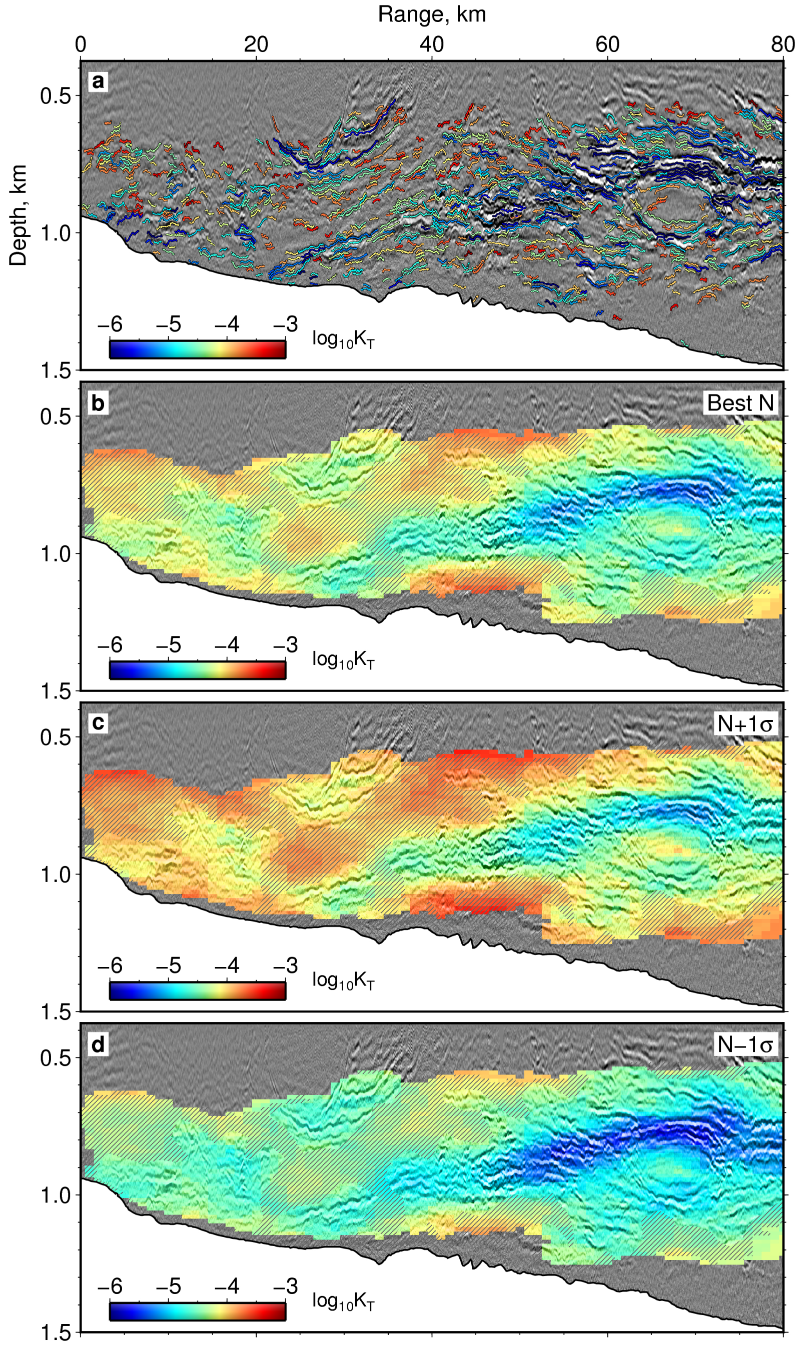

FIG. 15. Spatial variation of K_T across seismic profile shown in Figure 4a. (a) Gray background = seismic image; sloping base = sea bed; highlighted events = tracked reflections colored according to calculated values of K_T (see scale bar). (b) Interpolated and smoothed variation of K_T, using average variation of N with depth shown in Figure 2 (i.e. $N \sim 1.3$ cph). Hashed pattern = regions where signal-to-noise ratio < 3.5. Note reduced values of K_T at crest of eddy on right-hand side and increased values over shallow/rugose bathymetry. (c) $N+1\sigma$ (~ 1.6 cph). (d) $N-1\sigma$ (~ 0.9 cph).

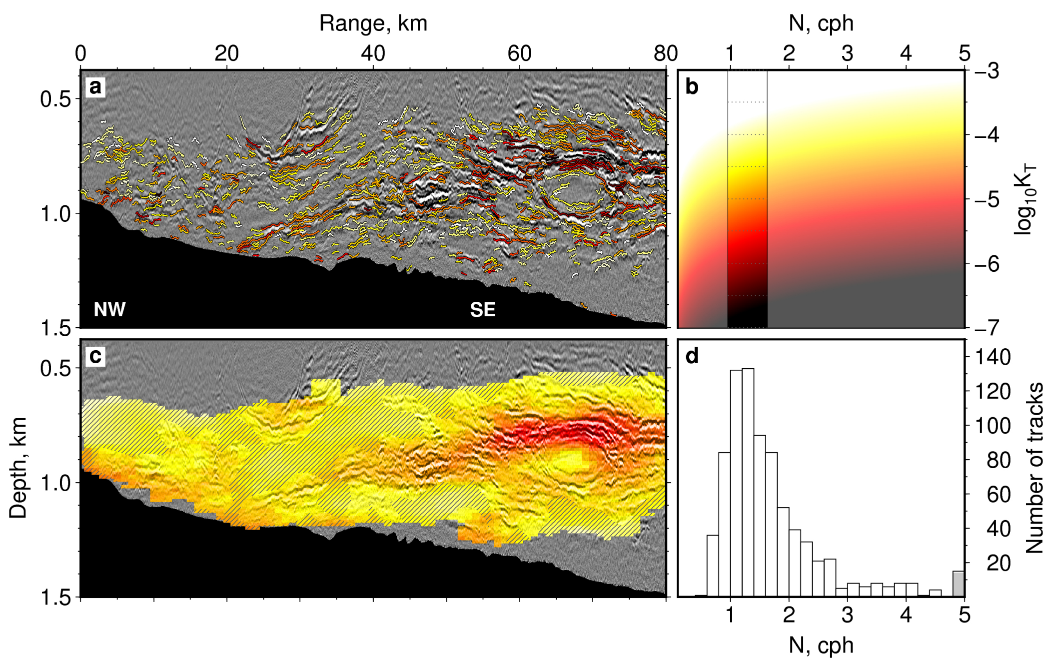

905 FIG. 16. Trade-off between K_T and N. (a) Gray background = seismic image; highlighted events = tracked reflections colored according to amplitude of turbulent regime of slope spectra. (b) Amplitude of turbulent regime as function of K_T and N. Highlighted band with horizontal dashed lines = range of values of K_T for $N \pm 1\sigma$. (c) Interpolated and smoothed variation of amplitude of turbulent regime. Hashed pattern = regions where signal-to-noise ratio < 3.5. (d) Histogram of number of tracked reflections as function of N for constant value of $\varepsilon = 10^{-10}$ m^{2}s^{-3}. Values of $N > 5$ are assigned to gray bin.